Journal of Materials Chemistry C

PAPER

View Article Online
View Journal | View Issue

Cite this: J. Mater. Chem. C, 2018, 6, 12728

Colorimetric detection and ratiometric quantification of mercury(II) using azophenol dye: 'dip & read' based handheld prototype device development†

Gagandeep Singh,[a] Pushap Raj,[a] Harupjit Singh[b] and Narinder Singh *[a]

The extreme toxicity of mercury and its derivatives results from its high affinity for thiol groups in proteins and enzymes, leading to the dysfunction of cells and consequent health problems. Thus, developing a rapid, cheap and colorimetric sensor for detecting mercury ions at very low levels remains a challenge. Herein, we have developed a new chromogenic azophenol-based probe which allows the colorimetric detection of Hg(II) metal ions and subsequently, showed suitability as a RGB chemodosimeter for the selective sensing of Hg(II) in aqueous medium. The UV-vis absorption and colorimetric study showed that the azophenol-based sensor is highly selective towards Hg(II) detection without the interference of other analytes. The color change from deep red to yellow in the complex solution after treating with mercury metal ions, which is visible by the naked-eye, makes this probe more convenient and simple to use in real sample analysis. Furthermore, for practical application of the sensor system in real time sample analysis, solid state silica based sensor chips have been developed which are impregnated with probe **1** displaying colorimetric changes for different concentrations of Hg^{2+}, where the intensity of the red color decreased gradually towards a yellow color after the addition of Hg^{2+}, apparently, makes them as potential candidate to conveniently monitor the concentration of Hg^{2+} in aqueous test solutions.

Received 18th September 2018,
Accepted 25th October 2018

DOI: 10.1039/c8tc04720k

rsc.li/materials-c

Introduction

In the last decade, the economies of developing countries have been booming, and the excessive number of industrial plants constructed in these countries has resulted in serious air/water pollution, and discharged toxic heavy metal ions may ultimately accumulate in human bodies through the food chain.[1] The widespread contamination with pollutants such as highly poisonous mercury species could jeopardize our ecosystem, imposing a great threat to human health.[2] Various neurological effects of mercury exposure have been mainly attributed to the organic form of mercury, predominantly methylmercury ($MeHg^+$), which is known to accumulate in the food chain and cross the blood brain barrier after human ingestion.[3] The literature reveals that there are very few colorimetric probes for $MeHg^+$, which is in strong contrast to the enormous interest in the detection of $MeHg^+$ in living systems.[4–6] It is well known that $MeHg^+$ acts physiologically by binding to sulfhydryl groups in proteins or cysteine, forming water soluble complexes in tissues. Since the recognition of the severe neurotoxic effects of mercury in the 1960s, the development of detection techniques for real-time and long-term monitoring of mercury contamination in environmental and biological samples has become a high priority. Accordingly various methods have been developed in the last couple of years, for instance, small organic molecules,[7,8] biomolecules,[9–11] and functionalized polymeric[12,13] and inorganic materials[14] have been used to construct optical sensors. Although such findings help to overcome the severity of organic mercury contamination, the threat of inorganic mercury, particularly mercury(II) ions, should not be underestimated. It is well established that due to bacteria-assisted biotransformation processes, mercury(II) ions are the "precursor" form of methylmercury.[15] The relevant speciation for Hg toxicity *via* drinking water is inorganic mercury in the form of labile Hg^{2+} ions. The World Health Organization and the U.S. Environmental Protection Agency (EPA) have set the guideline for the tolerable limit of mercury in drinking water at 30 and 10 nM, respectively.[16]

The development of sensitive and selective chromogenic sensors composed of chelating ligands that are used to detect

[a] Department of Chemistry, Indian Institute of Technology Ropar (IIT Ropar), Rupnagar, Punjab 140001, India. E-mail: nsingh@iitrpr.ac.in; Tel: +91-1881242176

[b] Centre for Biomedical Engineering, Indian Institute of Technology Ropar (IIT Ropar), Rupnagar, Punjab 140001, India

† Electronic supplementary information (ESI) available. CCDC 1859342. For ESI and crystallographic data in CIF or other electronic format see DOI: 10.1039/c8tc04720k

heavy-transition-metal cations in biological environments has attracted extensive scientific interest.[17–30] Chelating agents are well known for inhibiting the toxic effect of heavy metals, for instance, particularly, ethylenediamine tetra acetic acid (EDTA), which normally inhibits the toxic effect of heavy metals, however, it has no inhibitory effect on the toxicity of mercury or may even increase it.[31] Besides the development of these types of various effective nanosensors working in the solution phase, there is still a lack of a sensing method in the solid state reaching a sensitivity below 1 pM which is in great need for practical applications. Therefore, a sensitive optical probe that can detect ppb levels of inorganic mercury in drinking water will be extremely useful for establishing the drinkability of water, especially in remote areas where sophisticated instrumentation for analysis of the metal content in water is not available. Although there are numerous reports on optical sensors for detecting Hg^{2+}, major shortcomings are related to their limited aqueous solubility and irreversibility. Very few sensors have a combination of high aqueous solubility and reversibility along with the requisite limit of detection.

Thus, the development of irreversible reaction based chemodosimeters for mercury has attained much attention.

Because of the strong thiophilic affinity of Hg^{2+}, fluorescent changes associated with mercury-promoted desulfurization reactions which include hydrolysis, cyclization, and elimination reactions have been used in the design of chemodosimeters for Hg^{2+}.[32–35] However, significant challenges still exist in this field. For instance, to drive these desulfurization reactions to completion, it is often necessary to use either elevated temperature or excess quantities of Hg^{2+}. Although, some other metal ions such as Ag^{+} and Pb^{2+} which are less thiophilic than Hg^{2+} can also promote the desulfurization reactions.[36,37] Therefore, optimal ratiometric chemodosimeters for Hg^{2+} must possess fast response times at ambient temperature and the ability to selectively and stoichiometrically detect Hg^{2+}. Herein, we report a novel azophenol dye-based Hg^{2+} chemodosimeter as a new advance in this field. Our design is based on the well-known reaction mechanism for mercury induced desulfurization followed by cyclization leading to a heterocyclic moiety.[38] This approach involves the reaction of the target analyte *viz.* Hg^{2+} cations with the molecular probe, called here the chemodosimeter, and is associated with significant chemical transformation which involves the formation of covalent bonds and results in the formation of a product differing from the starting chemodosimeter concomitantly with optically different properties. This type of chemical transformation, achieved by the specifically designed reaction, is relatively less affected by the environment and provides a distinct advantage in terms of high selectivity. Earlier, Tae *et al.* reported that a rhodamine-based thiosemicarbazide was easily transformed into 1,3,4-oxadiazole in the presence of a Hg^{2+} ion,[7] and Tian *et al.* also used this desulfurization reaction to develop a naphthalimide-based chemodosimeter for the Hg^{2+} ion with a sensitive ratiometric signal from green to blue emission.[38] Therefore, in order to get better signal response, we use the azophenol dye chromophore to give rise to a sensitive and sharp color change which can be evaluated in terms of RGB based observation. Colorimetric sensors are well established as an economical and easily miniaturized alternative, where light is separated into a set of colors, primarily red (R), green (G), and blue (B). Thus, we demonstrate that the measurements can be carried out using conventional RGB sensors or on a smartphone application in terms of RGB values of 8-bit resolution (256-bit color scale with 255, 255, 255 corresponding to white, and 0, 0, 0 corresponding to black) circumventing all the limitations around the optical measurements with spectrometers and the data is frequently presented in terms of total color differences (ΔC) using the equation

$$\Delta C = \sqrt{(\Delta R)^2+(\Delta G)^2+(\Delta B)^2}$$

where: ΔR, ΔG, and ΔB are the change in red, green, and blue colors from reference values, respectively.

Experimental section

General information

All chemicals used were of analytical grade and were purchased from Sigma-Aldrich Co. ^{1}H and ^{13}C NMR spectra were recorded on an Avance-II (Bruker) instrument, which operated at 400 MHz for ^{1}H-NMR and 100 MHz for ^{13}C-NMR (chemical shifts are expressed in ppm). All chemical shifts were recorded in ppm relative to tetramethylsilane as an internal reference. The particle size of nano-aggregates was determined with Dynamic Light Scattering (DLS) using the external probe feature of a Metrohm Microtrac Ultra Nanotrac particle size analyzer. The photo-physical properties and recognition properties of the receptor and complex were determined with a Shimadzu UV-2400 spectrophotometer. The pH measurements were carried out on an ME/962P instrument. Mass spectra (HRMS) were analyzed on a Q-TOF high resolution mass spectrometer. The TEM images were recorded on a Hitachi (H-7500) instrument working at 120 kV.

Synthesis of probe 1

Initially, to prepare 4-nitrobenzenediazonium chloride, aromatic amine (0.01 mol) was dissolved in a 1 : 1 ratio of conc. HCl and water. Sodium nitrite solution (0.02 mol mL^{-1}) was added to the reaction mixture dropwise with continuous stirring. The reaction mixture was stirred for 45 min at a temperature of 0–5 °C. Then the diazotization step was followed by coupling of the diazotized amines by drop wise addition to a solution of salicylaldehyde (0.01 mol of salicylaldehyde dissolved in a 0.02 mol mL^{-1} solution of sodium hydroxide). The reaction was stirred at 0–5 °C for 2 hours under alkaline conditions. The conjugates of salicylaldehyde and aromatic amines were obtained as orange to red powders after the pH was neutralized to 6–7. Then, the condensation of *N*,*N*-dimethylethylenediamine and obtained 5-(2-(4-nitrophenyl)diazenyl)-2-hydroxybenzaldehyde results in the formation of schiff base compound **3**, which was further subjected to reduction with $NaBH_4$ in methanol affording compound **2**. The progress of the reaction was monitored using thin layer chromatography. After completion of the reduction,

the solvent was evaporated and the dark red crude compound **2** was obtained and purified with column chromatography. Further, the reaction of compound **2** (100 mg, 0.215 mmol) was carried out with phenyl isothiocyanate (120 mg, 0.645 mmol) in 15 mL dry DCM under refluxing for 8 h, which leads to the formation of the precipitated product probe **1**, which was characterized by rigorous spectroscopic analysis (^{1}H NMR, ^{13}C NMR and HRMS).

2-(((2-(Dimethylamino)ethyl)amino)methyl)-4-((4-nitrophenyl)-diazenyl)phenol (2). R_f 0.33 ($CHCl_3$/hexane 8 : 2); dark red powder, yield = 75%.

^{1}H NMR ($CDCl_3$, 400 MHz): δ 8.32 (m, 2H, Ar-H), 7.92 (m, 2H, Ar-H), 7.83 (m, 1H, Ar-H), 7.67 (s, 1H, Ar-H), 6.92 (m, 1H, Ar-H), 5.34 (br s, 2H, OH and NH), 4.09 (s, 2H), 2.73 (t, 2H, J = 6.0 Hz), 2.46 (t, 2H, J = 6.0 Hz), 2.23 (s, 6H, $CH_3 \times 2$).

^{13}C NMR ($CDCl_3$, 100 MHz): δ 163.74, 156.27, 148.05, 145.76, 126.10, 124.80, 123.54, 123.11, 123.01, 117.33, 57.85, 52.11, 45.56, 29.78.

HRMS (ESI, m/z): calculated for $C_{17}H_{22}N_5O_3$ $[M + H]^+$, 344.1723, found 344.1702.

1-(2-(Dimethylamino)ethyl)-1-(2-hydroxy-5-((4-nitrophenyl)-diazenyl)benzyl)-3-phenylthiourea (1). R_f 0.30 ($CHCl_3$/hexane 7 : 3); red powder, yield = 70%.

^{1}H NMR ($CDCl_3$, 400 MHz): δ 12.6 (s, 1H, NH), 8.37–8.34 (m, 2H, Ar-Hs), 7.97 (m, 3H, Ar-Hs), 7.76 (dist s, 1H, OH), 7.34–7.32 (m, 5H, Ar-Hs), 7.18–7.14 (m, 1H, Ar-H), 7.08–7.06 (m, 1H, Ar-H), 5.25 (s, 2H, CH_2), 3.60–3.58 (m, 2H, CH_2), 2.72 (m, 2H, CH_2), 2.39 (s, 6H, N-$CH_3 \times 2$).

^{13}C NMR ($CDCl_3$, 100 MHz): δ 183.50, 161.65, 156.15, 148.25, 145.78, 140.50, 128.82, 128.77, 126.08, 125.20, 124.85, 124.11, 123.09, 121.53, 118.78, 58.93, 53.93, 47.44, 45.43.

HRMS (ESI, m/z): calculated for $C_{24}H_{26}N_6O_3S$ $[M + H]^+$, 479.1865, found 479.1840.

Synthesis of ONPs of probe 1

It is well established that the developed bio-analytical technique is more powerful if it works efficiently in aqueous medium. Thus, the fabrication of ONPs is generally governed by the field of application. The solubility difference of the compound in aqueous/organic solvent is the influencing factor for the fabrication of ONPs. In the present investigation, organic nanoparticles were prepared by the re-precipitation method. Probe **1** was dissolved in DMSO and slowly injected into water with sonication. After the injection, sonication was continued for another 30 min to ensure the preparation of stable organic nanoparticles. Nanoparticle formation was examined using an external probe for particle size analysis. The size distribution of the ONPs was continuously analyzed using DLS, whereas, the size and shape of ONPs were studied through TEM analysis.

Recognition studies

UV-vis absorption spectral profiles were recorded at 25 ± 1 °C. The solutions were shaken sufficiently and sonicated before recording the spectrum. The binding behavior of the organic nanoparticles formed from probe **1** was first studied for various cations and anions. Before the spectra were recorded, the volumetric flasks were allowed to stand for half an hour. For the assessment of the effect of ionic strength, the spectrum was recorded at different concentrations of various TBA salts (0–100 equiv.). pH titrations were also performed to explore the effect of pH on the recognition behavior by varying the acidity and basicity of the solution.

Determination of mercury in water and plant samples

Various water samples from a tap on campus and water from a nearby pond and river were used for environmental sample testing. Sample solutions were collected and then filtered 3 times through a filter with a pore size of 0.2 μm. Hg^{2+} at concentrations over the range of 2–40 μM was spiked into the pond and river water samples. The detection processes are identical to those mentioned above for recognition studies. On the other hand, for plant samples, the selected fresh plant samples were cleaned with Milli-Q water, and the fresh weight (FW) of the samples was recorded. Each individual plant sample was separated into root, stem and leaf sub-samples. All the collected sub-samples were air-dried, weighed to record the dry weight (DW) and then ground to a fine powder and passed through a 0.18 mm-mesh sieve and stored in polythene zip-bags at ambient temperature. Then for analysis, the dried and pulverized samples were subjected to digestion according to the method reported earlier (EPA method 7473) with some modifications. Further, to avoid any external contamination, all the sample processing was performed in a laminar flow fume cupboard. The final concentrations of mercury in plant samples were analyzed using absorption spectrophotometry. The results were analyzed with analyses of variance.

Handheld device design for RGB analysis

The 3D drawing of the sample holder was created using Free CAD which is a free and open-source general-purpose parametric 3D CAD modeler. The outer dimensions of the holder were fixed at 133.8 mm × 68.6 mm × 100 mm ($L \times W \times H$) by keeping in mind the dimensions of a cell phone (iPhone SE). The main holder is divided into two compartments where one compartment contains a square pocket (30 × 30 mm) at the bottom for holding samples (Sensor Chip) and the other compartment houses the electric circuit components. The holder was printed using the Dimension uPrint SE Plus 3D printer and the printing filament was made of ABS (acrylonitrile butadiene styrene). In order to fix all the lighting conditions, the top of the holder was cut out in such a way that the smartphone fit perfectly and did not allow external light to enter the sample compartment. Two white light emitting diodes were fitted in the sampling compartment for lighting the sample with constant intensity. A two position on off switch was housed in the circuit compartment which allowed turning on and off the LEDs. A 9 V battery was utilised for powering the LED lights. Then digital pictures were taken by the iPhone SE camera, and analysed for RGB components by a freely downloaded application from the iOS App Store *i.e.* Pixel Picker.

Results & discussion

Synthesis and characterization of the organic receptor

The synthetic protocol employed for the preparation of target receptor **1** is illustrated in Scheme 1. The azodye coupled

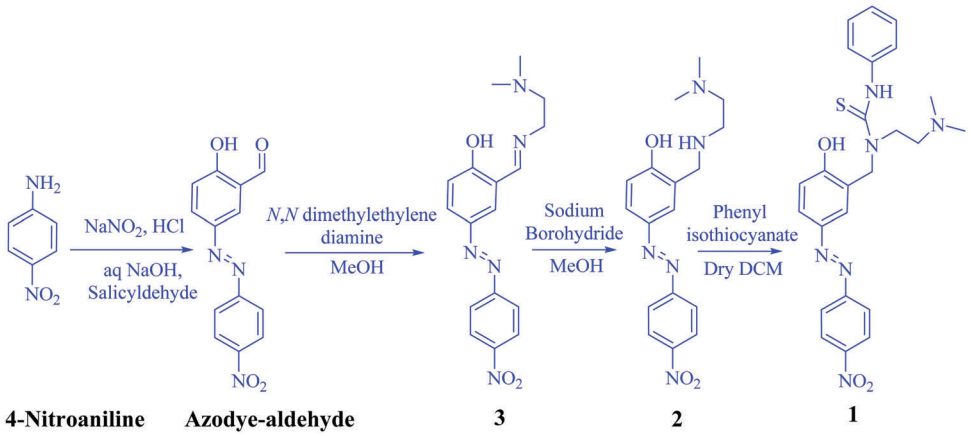

Scheme 1

aldehyde was prepared using the literature method.[39] The condensation reaction between the obtained azo-aldehyde and *N*,*N*-dimethylethylenediamine yielded the imine linked receptor (**3**; Fig. S_1 and S_2, ESI†), which was further subjected to reduction with $NaBH_4$ in methanol. This afforded compound **2** (Fig. S_3–S_6, ESI†) in good yield, which was further reacted with phenyl isothiocyanate leading to the formation of probe **1**; characterized with spectroscopic techniques such as ^{1}H NMR, ^{13}C NMR and HRMS (Fig. S_7–S_9; ESI†). Probe **1** is designed in such a way that it has oxygen, nitrogen and sulphur donor sites along with an optical-signaling chromophore unit (azophenol moiety) to selectively trigger color change upon complexation with the analyte.

The ^{1}H NMR spectrum of probe **1** showed signals at δ 12.6 ppm and 7.76 ppm (exchangeable with D_2O) ascribed to NH (thioamide) and OH (azophenol dye) protons, respectively. Resonances at δ 3.60 (m, 2H, CH_2), δ 2.72 (m, 2H, CH_2), and δ 2.39 (s, 6H, $CH_3 \times 2$) were indicative of the presence of the *N*,*N*-dimethyl ethyl chain, and the structure was also corroborated by ^{13}C NMR spectral assignments. The peak corresponding to the mass of probe **1** with *m*/*z* 479.1840 (calc. *m*/*z* 479.1865) was observed in HRMS, confirming the molecular formula for the assigned structure, which was also supported by proton–carbon connectivities *via* the HSQC spectrum. Overall ^{1}H and ^{13}C NMR spectral assignments, aided by ^{1}H–^{13}C hetero-COSY experiments, corroborated the assigned structure. Finally, the structure of probe **1** was established by X-ray crystallography (Fig. 1).[40]

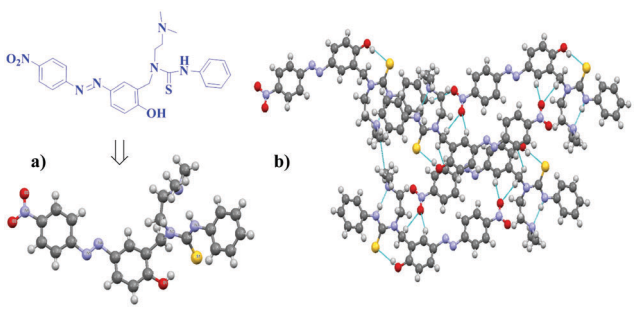

Fig. 1 (a) ORTEP view of probe **1**; (b) packing arrangement of probe **1** viewed down the *b*-axis.

Table 1 Crystal data and structure refinement for probe **1**

Empirical formula	$C_{24}H_{26}N_6O_3S$
Formula weight	478.57
Temperature/K	273.15
Crystal system	Triclinic
Space group	$P\bar{1}$
a/Å	9.1010(4)
b/Å	9.2238(4)
c/Å	14.9779(7)
α/°	80.357(2)
β/°	89.219(2)
γ/°	82.426(2)
Volume/Å^3	1228.71(10)
Z	2
ρ_{calc}/g cm^{-3}	1.294
μ/mm^{-1}	0.169
F(000)	504.0
Crystal size/mm^3	0.4 × 0.3 × 0.2
Radiation	MoKα (λ = 0.71073)
2*Θ* range for data collection/°	4.518 to 56.57
Index ranges	$-12 \le h \le 12$, $-12 \le k \le 12$, $-19 \le l \le 19$
Reflections collected	36 352
Independent reflections	5996 [R_{int} = 0.0486, R_{sigma} = 0.0417]
Data/restraints/parameters	5996/0/310
Goodness-of-fit on F^2	1.033
Final *R* indexes [$I \ge 2\sigma(I)$]	R_1 = 0.0887, wR_2 = 0.1992
Final *R* indexes [all data]	R_1 = 0.1251, wR_2 = 0.2139
Largest diff. peak/hole/e Å^{-3}	1.36/−0.73

Probe **1** crystallizes in the triclinic crystal system with the $P\bar{1}$ space group, where the asymmetric unit consists of one moiety of probe **1**. The crystal structure diagram along with atom numbering for probe **1** is given in Fig. 1a. Probe **1** is stabilized by O–H···S and NH···N intramolecular hydrogen bonding and the selected bond lengths and bond angles are given in Tables S_1–S_3 (ESI†). The moieties of probe **1** are arranged in the form of a one-dimensional chain running along the *b*-axis. Different moieties in these chains are joined together by the O–H···C/CH···O type of hydrogen bonds as shown in Fig. 1b. The crystal refinement parameters are given in Table 1.

Preparation of organic nanoparticles of probe 1

Due to the poor aqueous solubility of probe **1**, it was decided to compare the photo-physical properties of probe **1** in an organic

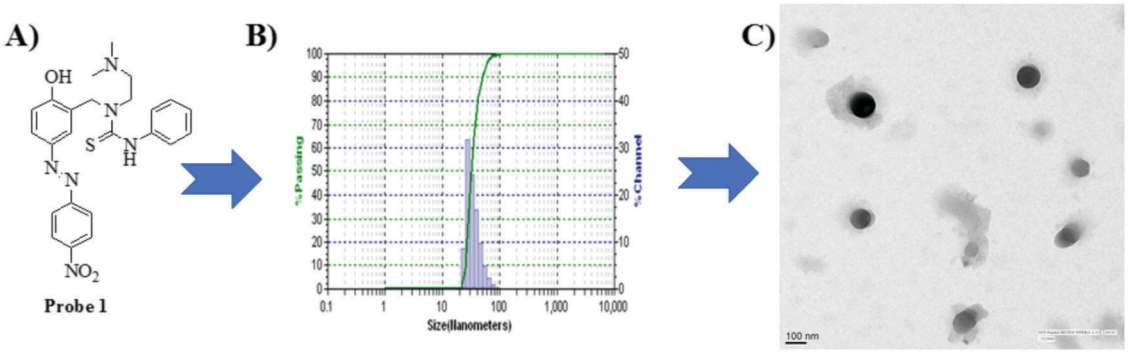

Fig. 2 (A) Chemical structure of probe **1**; (B) DLS histogram of probe **1** (ONP) showing a particle distribution under 65–75 nm; (C) TEM image showing the formation of organic nanoparticles (ONPs) of receptor **1** in the DMSO/H_2O (1 : 99, v/v) solvent system.

solvent such as DMSO, DMF and acetonitrile, and compare the functioning of probe **1** in a semi-aqueous medium with a varied fraction of water even up to 99% of water *i.e.* DMSO/H_2O (1 : 99, v/v), to make the developed analytical technique more powerful and efficient in aqueous medium. Consequently, organic nanoparticles (**N1**) of probe **1** were prepared with DMSO, DMF and acetonitrile for its real time applicability in aqueous medium using the re-precipitation method. The size range of the obtained organic nanoparticles was confirmed by using the dynamic light scattering method (DLS) and the hydrodynamic size distribution of ONPs was observed under a 65–75 nm range for the DMSO/H_2O system (1 : 99, v/v; Fig. 2B), which is lesser than the size expressed from the TEM image (about 90 nm; Fig. 2C), whereas, for both other DMF/H_2O and ACN/H_2O solvent systems, the particle size is much higher as compared to the DMSO/H_2O system (Fig. S_{10} and S_{11}, ESI†).

Photo-switching studies, influence of pH values and ionic strength on the stability of prepared probe 1 in an aqueous solution. Azobenzenes are well-known for their characteristic optical absorption properties and are, perhaps, the most widely studied photo switchable systems,[41–48] thus the obtained probe **1** was initially investigated for its *cis–trans* behavior *via* UV-visible absorption spectroscopy. It is well established that azo-based compounds undergo *trans*-to-*cis* conversion under UV irradiation, while the reverse process occurs under visible light or *via* thermal relaxation.[49–53] Literature reports also revealed that *p*-hydroxy-substituted azo derivatives exhibit the typical spectral profile of azobenzenes, *i.e.* a strong band with a maximum between 350 and 380 nm, assigned to the symmetry-allowed π–π* transition of the *trans* isomer, and a weaker broad band peaking at *ca.* 450 nm, associated with a symmetry-forbidden n–π* transition.[44] For photo-switching studies in solutions, probe **1** was dissolved in acetonitrile at suitable concentration. The UV-vis absorption spectrum was recorded using a Shimadzu UV-2400 spectrophotometer. To study the *cis–trans* isomerisation of probe **1** in ACN (Fig. S_{12}, ESI†), a solution of this compound was irradiated with UV light at 365 nm for 20 minutes, after which the formation of the absorption spectrum for the *cis* isomer was observed by UV-visible spectroscopy. The UV irradiated solution was then kept in the dark to allow the *cis–trans* thermal isomerisation to take place. This process was followed by periodically recording UV-visible spectra of probe **1**. It was observed that there is no change in absorbance shift after irradiation with UV light, however, indicating only enhancement in absorbance that exhibits an intense π–π* transition band at 370 nm and a weak n–π* absorption band at 470 nm. Increasing formation of the band at 370 nm was observed with a decrease of the band at 470 nm over time (Fig. S_{13a}, ESI†), indicating that the formation of the *trans* isomer was proceeding. After 12 hours of relaxation in the dark, the *trans* isomer of probe **1** was regenerated indicating little degradation during the photo switching process. Probe **1** can also undergo tautomerisation as illustrated in Fig. 3, to form a tautomer that can freely rotate, which may make the rate of *cis–trans* reversion very fast.

Further, for *trans* to *cis* photo isomerism, a solution of probe **1** in ACN was continuously irradiated with UV light at 365 nm for 20 min. UV-visible absorption spectra of probe **1** are shown in Fig. S_{13b} (ESI†). The process was monitored by recording UV-visible spectra of the sample periodically. It was observed that the absorbance of the band at 362 nm decreased with hypsochromic shift and an increase in absorbance for the band at 470 nm, and the latter absorbance has previously been attributed to the *cis* isomer. The UV-visible spectrum of probe **1** after 20 min of irradiation also showed an absorption band at 320 nm. Thus, *cis–trans* isomerisation for probe **1** was observed to be much faster, and it is well known that in terms of application in photo switches, azo compounds that exhibit fast isomerisation are of most interest, suggesting probe **1** would be a good candidate in this context.

A suitable pH range for detection of required or desired analytes is a key factor to consider in real application. Thus,

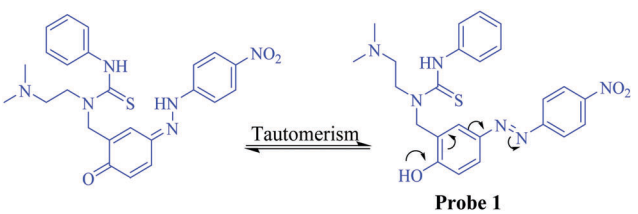

Fig. 3 Tautoisomerization in probe **1**.

to understand the effects of aquatic conditions on the prepared azo-dye based probe **1** for the detection of Hg^{2+}, we have investigated the stability of prepared organic nanoparticles under different pH conditions (Fig. S_{14a}, ESI†). The UV-visible absorption spectra remain unchanged within a wide pH range covering physiological pH. These results show that probe **1** works efficiently at physiological pH (pH 5–8) and can be applied suitably for detection of Hg^{2+} in real samples, such as in waste water and industrial analysis. An experiment was also conducted to see the effect of high ionic strength. Therefore, tetrabutylammonium salts were added (0–100 μM concentrations) to the probe **1** complex solution, however, no significant change was observed in UV-visible absorption spectra (Fig. S_{14b}, ESI†). Thus, probe **1** exhibited good stability under a wide pH range with no hindrance from the salts present in the environment and this feature proves its practical application for the determination of other analytes in aqueous medium.

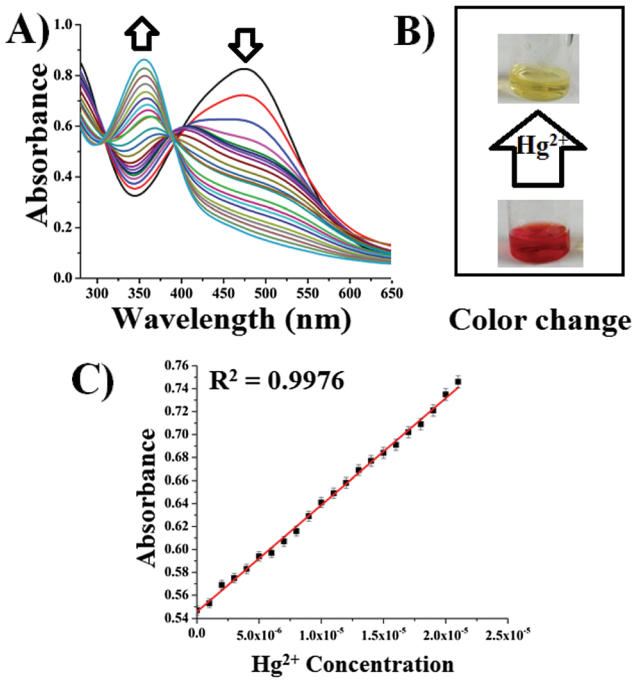

Fig. 4 (A) Modulation of the UV-visible absorption band of probe **1** upon successive addition of Hg^{2+} metal ions (0–10 μM) in the DMSO/H_2O (1 : 99, v/v) solvent system; (B) color change from red to yellow after the addition of Hg^{2+} metal ions; (C) linear regression graph showing the change in absorption intensity with respect to the concentration of Hg^{2+} metal ions.

Ultrasensitive and selective detection of Hg^{2+} ions

Further, upon the addition of Hg^{2+} ions into probe **1** nanoparticles, apparent changes in the UV-visible absorption spectra can be observed from Fig. 4A, which shows the change in absorption intensity as well as in color, from red to yellow, which can be easily detected with the naked eye (Fig. 4B) in the presence of Hg^{2+} ions (0–10 μM) in phosphate buffered saline (PBS, 10 mM, 7.4) buffer solution. This clearly indicates that probe **1** is a highly selective colorimetric sensor for Hg^{2+} ions. It was also observed that the absorption peak at λ_{max} 477 nm disappeared and a new absorption peak at λ_{max} 354 nm appeared with gradual addition of Hg^{2+} metal ions (0–10 μM; Fig. 4A), and the linearity was determined to be 0.9976. The detection limit was 8.1 nM based on S/N = 3. Consequently, an isosbestic point at λ_{max} 393 nm was also observed which clearly indicates the complex formation due to complexation between probe **1** and Hg^{2+} metal ions. The selective behavior of probe **1** under study can be attributed to the complementarity of the soft sulphur binding site as shown earlier. Additionally, to the solution of probe **1**, various other metal salts have also been added along with Hg^{2+}, inducing the same absorption changes in its response to Hg^{2+}, indicating a negligible interference effect from other metal ions on the recognition performance of probe **1** (Fig. S_{15}, ESI†).

Next, in order to rationalize the interaction of probe **1** with Hg^{2+} metal ions (Fig. 5), and to study the binding ratio between Hg^{2+} and probe **1**, ESI mass spectra were recorded for probe **1** with the addition of Hg^{2+} ions (1 equiv.) to the probe **1** solution, which showed an appearance of a signal at m/z 445.17 rapidly, attributed to the molecular ion $[\mathbf{4} + H]^+$ peak, while the peak at m/z 479 (molecular ion $[\mathbf{1} + H]^+$) decreased (Fig. S_{16}, ESI†), directly revealing that the binding stoichiometry of probe **1** with Hg^{2+} ions was 1 : 1. At higher values, various ion peaks with weak intensities are found which are attributed to the presence

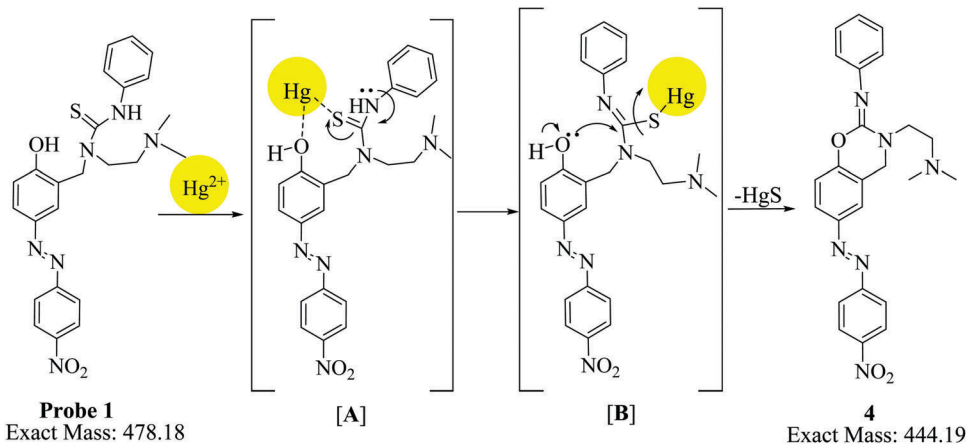

Fig. 5 Tentative mechanism for desulfurization of probe **1**.

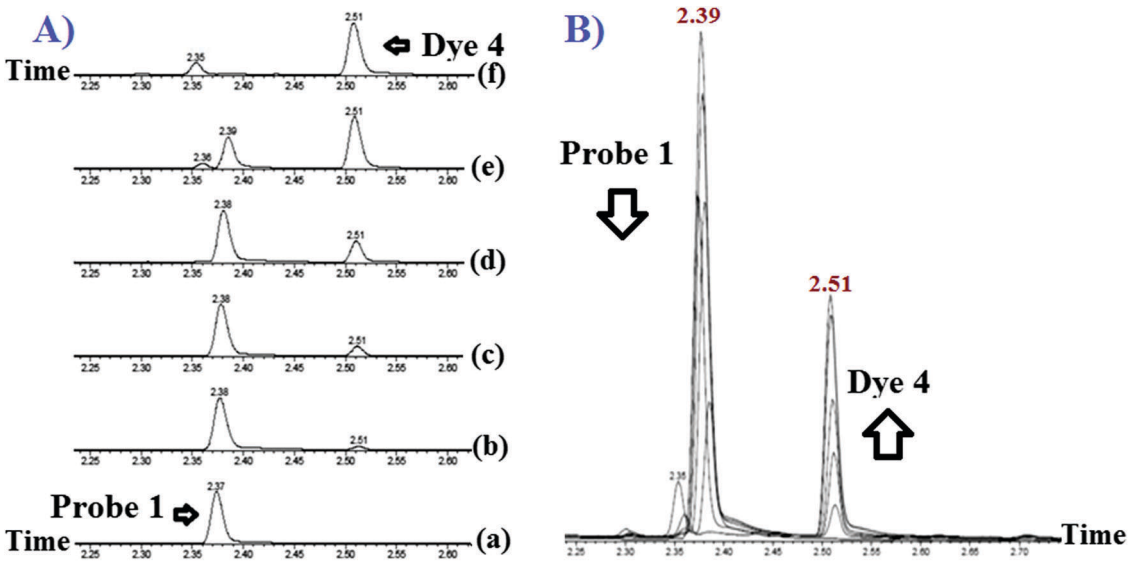

Fig. 6 LC-MS chromatograms: (A) probe **1** (10.0 μM) after addition of 0–2.0 equiv. of Hg^{2+} (b–f); (B) overlay representation of LC-MS chromatograms.

of cluster ions only; *i.e.*, there is no evidence for the formation of a Hg^{2+} complex that can be isolated.

To further confirm the sensing mechanism (Fig. 5), LC-MS analysis was also performed on probe **1** with gradual addition of Hg^{2+} to the probe **1** solution. Probe **1** and obtained dye **4** exhibited a single peak with retention times at 2.37–2.39 min (Fig. 6a) and 2.51 min (Fig. 6d), respectively. When 0.2 equiv. of Hg^{2+} was added into the solution of probe **1**, the intensity of the peak at 2.38 min decreased with a concomitant occurrence of a new peak at 2.51 min (Fig. 6b–e). The gradual addition of an excess of Hg^{2+} (up to 2.0 equiv.) into the solution of probe **1** resulted in the complete disappearance of the peak at 2.37–2.39 min and only one peak at 2.51 min remained (Fig. 6f), which is attributed to dye **4** as confirmed by its mass also.

Furthermore, to support and understand theoretically the binding mechanism for probe **1** and Hg^{2+} complexation leading to the formation of dye **4**, keeping in mind that the strong thiophilic affinity of Hg^{2+} might lead to desulphurization and recyclization in intermediates [**A**] and [**B**] as depicted in Fig. 5, the energies of the highest occupied molecular orbital (HUMO) and lowest unoccupied molecular orbital (LUMO), and energy gaps were calculated for probe **1**, and dye **4**, by using DFT (density functional theory); the calculations were performed using GGA-DFT package DMol-36. The energies of the HOMO and LUMO characterize the electron donating and accepting abilities, respectively, whereas, the HOMO–LUMO gap is related to the chemical stability/reactivity of a molecule. The HOMOs and LUMOs of the reactant/product state analogs are shown in Table S_4 (ESI†), which clearly reveals that the HOMO–LUMO gaps for both probe **1** and dye **4** are very comparable to each other and thus, are stable in nature.

Determination of mercury in real water/plant samples

Particularly in developing countries, aside from some natural calamities, the burning and use of coal in industrial processes such as mining and petrochemicals is the main cause of mercury pollution.[54] The use of mercury-containing pesticides, household bleach, caustic chemicals, and mercury-contaminated irrigation water can also lead to the absorption and enrichment of mercury in agricultural products.[55–57] Thus, in order to explore the real application of probe **1**, we have utilized it to quantitatively determine Hg^{2+} in tap water, Sutlej River water and pond water samples collected from near the Ropar region. All the water samples under investigation were collected from three different sites near to the Ropar region and filtered through a 0.25 μM filter membrane prior to the experiment, and then were spiked with different concentrations of Hg^{2+} (2 to 40 μM). It's been observed that there is a linear relationship between the absorption at 354 nm and Hg^{2+} concentration in real water samples (Fig. 7a–d) with a good recovery (Table S_5, ESI†).

In addition, the potential application of probe **1** in detecting Hg^{2+} in plants was also evaluated. Literature studies revealed that plants can absorb mercury from both air and soil.[58–60] Which part of the plant gets more contaminated with mercury is entirely dependent upon the route of exposure of mercury. For instance, when plants absorb mercury from the soil, the mercury content should be higher in the roots; whereas, the mercury contents should be higher in shoots and leaves if air mercury is the main source of mercury contamination. Thus, for the detection of mercury and its accumulation in different parts of a selected plant (*i.e.* money plant), which is grown in the laboratory with spiked soil samples of Hg^{2+}, we have measured the mercury concentrations *via* absorption spectroscopy in leaves, stems, and root extract of the money plant (*Epipremnum aureum*). The results demonstrate the potential utility of probe **1** in real sample analysis which reveals that the mercury contents were much higher in roots than in stems and leaves (Fig. 8).

RGB analysis for chromogenic sensing

Keeping in mind the sharp color change of probe **1** from red to yellow (Fig. 4b) by the addition of Hg^{2+} in the solution phase,

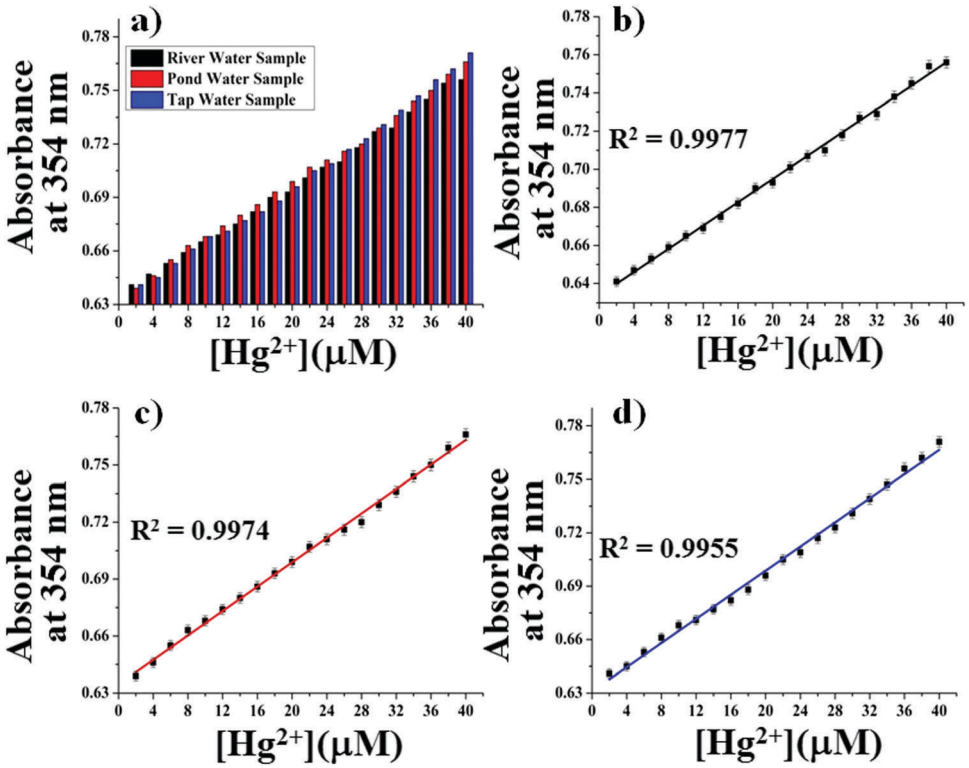

Fig. 7 (a) UV-visible absorption response of probe **1** (10.0 μM) in the presence of different concentrations of Hg^{2+} ions in real water samples; linear relationships of absorption of probe **1** at 354 nm *versus* the spiked concentration of Hg^{2+} (0.0–40.0 μM) in (b) river water, (c) pond and (d) tap water samples.

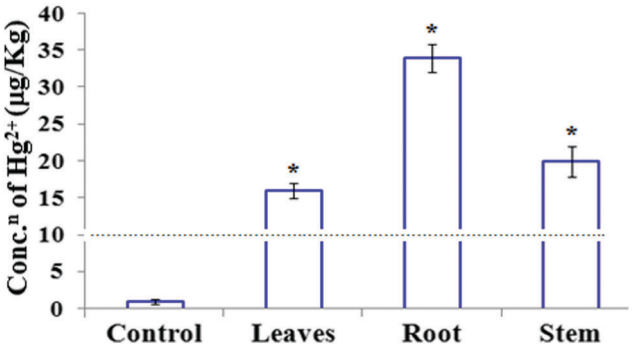

Fig. 8 Mercury distribution in organs of the *Epipremnum aureum* plant grown in Hg^{2+} spiked soil in lab conditions. Dashed line: maximum allowed mercury level in vegetables (10 μg kg^{-1} FW) (Food Safety Standard).

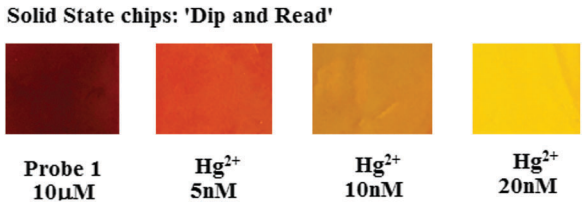

Fig. 9 Visible color changes in solid state chips: untreated silica chip impregnated with probe **1**, and after treatment with varied concentration of Hg^{2+}.

it was decided to investigate the developed probe **1** in the solid silica phase also, in order to develop a simple, portable, and affordable detection system that would significantly improve the ease of detection of heavy metal contamination in remote locations. Thus, small size (4 × 4 cm) silica chips were dipped in a solution of probe **1** in CH_3CN (2 mL, 10 μM) and air dried which results in red colored silica chips (Fig. 9). Then these prepared red colored probe **1** impregnated silica based sensor chips were treated with varied concentration solutions of Hg^{2+} (1–20 nM) in double distilled water resulting in instant color change from red to yellow (Fig. 9). As the color change was rapid and clearly detected, probe **1** can also be used for practical applications in the solid state. Low naked eye detection *via* solid state silica based sensor chips coated with chemo-dosimeter probe **1** makes them a potential candidate to conveniently monitor the concentration of Hg^{2+} metal ions in aqueous solution.

Nowadays, smartphones are portable, widely available, user-friendly, and therefore well suited to act as an effective platform for on-site detection.[61–63] Many interesting biosensors have been designed based on smartphones utilizing mobile apps and various connected devices, such as high-performance cameras and light sensors.[64,65] Thus, inspired by sharp color changing results from our developed solid sensor chips with Hg^{2+} (Fig. 9), herein, we have developed a battery-powered mobile sensing device that consists of a lightweight (~20 g) opto-mechanical attachment to a smart-phone along with an application for collecting, reporting and sharing RGB data, in order to provide

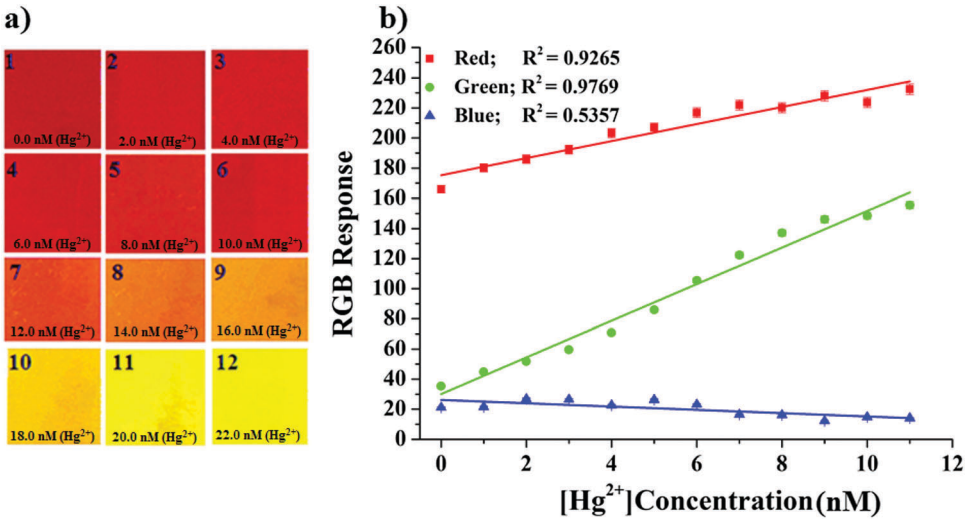

Fig. 10 (a) Digital images of the probe **1** solution taken by the iphone SE rear camera after addition of different concentrations of Hg^{2+} metal ions; (b) RGB responses extracted from digital images of the probe **1** solution after addition of varied concentration of Hg^{2+} metal ions.

a field-portable, economic, and wirelessly connected platform to perceptibly quantify Hg^{2+} metal ion concentration in water samples (Fig. S_{17}, ESI†). This lab-on a-phone device is based on fixed wavelength illumination using light-emitting diodes (LEDs) and can quantify mercury-induced subtle transmission changes of a colorimetric assay utilizing solid state silica based chips impregnated with probe **1**. A series of experiments were conducted with Hg^{2+} solutions in the concentration range of 1–20 nM. Digital images for the color changes after addition of Hg^{2+} metal ions to the solution of probe **1** are displayed in Fig. 10. As shown in Fig. 10, sample spots are shown from red, through orange to yellow, and the colors gradually became sharp in their intensity as the Hg^{2+} concentration increased. According to the color wheel theory, the color shown by the object is the complementary color of that which is absorbed by the object, *i.e.* here the solution sample appears red, through orange to yellow, because the red to yellow color is transmitted by the sample and the complementary color, the blue part of the spectrum, is absorbed, as revealed by the UV-visible spectrum also, which is attributed to blue light. The RGB responses of the digital images were extracted and are illustrated in Fig. 10. From each part of Fig. 10b, it can be seen that there is an increase in the value of the G-component and a decrease in the value of the B-component with the increase of Hg^{2+} ion concentration. On the basis of the linear relationship between the RGB data and Hg^{2+} concentration, the limit of detection, which corresponds to the signal-to-noise ratio, was determined to be 13 nM which was very comparable with the maximum tolerable level (10 nM) for Hg^{2+} in drinking water permitted by the United States Environmental Protection Agency, whereas, lower than the WHO permitted standards (30 nM).

Conclusion

In the present investigation, we have designed and synthesized a novel chromogenic azophenol-based chemodosimeter which allows the colorimetric detection of Hg^{2+} metal ions in an aqueous medium with high selectivity and sensitivity. The mass spectroscopy clearly shows 1 : 1 binding stoichiometry ratios of probe **1** with Hg^{2+}, which was also corroborated by LC-MS analysis. The UV-visible absorption spectrum clearly revealed that the absorption peak at λ_{max} 477 nm for probe **1** disappeared and a new absorption peak at λ_{max} 354 nm appeared with gradual addition of Hg^{2+} metal ions. Consequently, an isosbestic point at λ_{max} 393 nm was also observed which clearly indicates the complexation between probe **1** and Hg^{2+} metal ions. Naked-eye sensing helped in observing the color changes in the complex solution, produced from the effect of mercury metal ions, thus making it more convenient to use in real sample analysis. Furthermore, for practical application of the sensor system in real time sample analysis, we have developed solid state silica based sensor chips coated with probe **1** which display colorimetric changes for different concentrations of Hg^{2+}, where the intensity of the red color decreased gradually towards a yellow color after the addition of Hg^{2+}, which makes them a potential candidate to conveniently monitor the concentration of Hg^{2+} in aqueous test solutions.

Conflicts of interest

There are no conflicts to declare.

Acknowledgements

Financial assistance in the form of sponsored research project PDF/2017/000414 by SERB, Department of Science & Technology, Government of India is gratefully acknowledged.

References

1 A. Singh and S. Prasad, *Int. J. Environ. Sci. Technol.*, 2015, **12**, 353–366.
2 Y. S. Hong, Y. M. Kim and K. E. Lee, *J. Prev. Med. Public Health*, 2012, **45**, 353.

3 T. W. Clarkson, *Crit. Rev. Clin. Lab. Sci.*, 1997, **34**, 369–403.
4 A. Ono and H. Togashi, *Angew. Chem.*, 2004, **116**, 4400–4402.
5 J. S. Lee, M. S. Han and C. A. Mirkin, *Angew. Chem., Int. Ed.*, 2007, **46**, 4093–4096.
6 C. W. Liu, C. C. Huang and H. T. Chang, *Anal. Chem.*, 2009, **81**, 2383–2387.
7 Y. K. Yang, K. J. Yook and J. Tae, *J. Am. Chem. Soc.*, 2005, **127**, 16760–16761.
8 S. Yoon, A. E. Albers, A. P. Wong and C. J. Chang, *J. Am. Chem. Soc.*, 2005, **127**, 16030–16031.
9 C. K. Chiang, C. C. Huang, C. W. Liu and H. T. Chang, *Anal. Chem.*, 2008, **80**, 3716–3721.
10 T. Li, S. Dong and E. Wang, *Anal. Chem.*, 2009, **81**, 2144–2149.
11 T. Li, B. Li, E. Wang and S. Dong, *Chem. Commun.*, 2009, 3551–3553.
12 D. E. Wylie, L. D. Carlson, R. Carlson, F. W. Wagner and S. M. Schuster, *Anal. Biochem.*, 1991, **194**, 381–387.
13 M. Matsushita, M. M. Meijler, P. Wirsching, R. A. Lerner and K. D. Janda, *Org. Lett.*, 2005, **7**, 4943–4946.
14 B. K. Jena and C. R. Raj, *Anal. Chem.*, 2008, **80**, 4836–4844.
15 J. D. Blum, B. N. Popp, J. C. Drazen, C. A. Choy and M. W. Johnson, *Nat. Geosci.*, 2013, **6**, 879.
16 G. H. Chen, W. Y. Chen, Y. C. Yen, C. W. Wang, H. T. Chang and C. F. Chen, *Anal. Chem.*, 2014, **86**, 6843–6849.
17 X. Zhu, W. Chen, K. Wu, H. Li, M. Fu, Q. Liu and X. Zhang, *New J. Chem.*, 2018, **42**, 1501–1509.
18 K. Wu, X. Zhao, M. Chen, H. Zhang, Z. Liu, X. Zhang, X. Zhu and Q. Liu, *New J. Chem.*, 2018, **42**, 9578–9587.
19 H. Liu, Y. Ding, B. Yang, Z. Liu, Q. Liu and X. Zhang, *Sens. Actuators, B*, 2018, **271**, 336–345.
20 K. Leus, K. Folens, N. R. Nicomel, J. P. H. Perez, M. Filippousi, M. Meledina, M. M. Dîrtu, S. Turner, G. Van Tendeloo and Y. Garcia, *J. Hazard. Mater.*, 2018, **353**, 312–319.
21 Y. Ding, S. Wang, J. Li and L. Chen, *TrAC-Trend Anal. Chem.*, 2016, **82**, 175–190.
22 L. Chen, J. Li and L. Chen, *ACS Appl. Mater. Interfaces*, 2014, **6**, 15897–15904.
23 L. Chen, X. Fu, W. Lu and L. Chen, *ACS Appl. Mater. Interfaces*, 2012, **5**, 284–290.
24 T. Lou, L. Chen, C. Zhang, Q. Kang, H. You, D. Shen and L. Chen, *Anal. Methods*, 2012, **4**, 488–491.
25 T. Lou, Z. Chen, Y. Wang and L. Chen, *ACS Appl. Mater. Interfaces*, 2011, **3**, 1568–1573.
26 G. Wang, Z. Chen, W. Wang, B. Yan and L. Chen, *Analyst*, 2011, **136**, 174–178.
27 L. Chen, T. Lou, C. Yu, Q. Kang and L. Chen, *Analyst*, 2011, **136**, 4770–4773.
28 J. Li, J. Liu, W. Lu, F. Gao, L. Wang, J. Ma, H. Liu, C. Liao and L. Chen, *Electrophoresis*, 2018, **39**, 1763–1770.
29 L. Wang, X.-J. Zhu, W.-Y. Wong, J.-P. Guo, W.-K. Wong and Z.-Y. Li, *Dalton Trans.*, 2005, 3235–3240.
30 W.-Y. Wong, *Coord. Chem. Rev.*, 2007, **251**, 2400–2427.
31 S. J. Flora and V. Pachauri, *Int. J. Environ. Res. Public Health*, 2010, **7**, 2745–2788.
32 J. C. Manimala and E. V. Anslyn, *Eur. J. Org. Chem.*, 2002, 3909–3922.
33 R. A. Batey and D. A. Powell, *Org. Lett.*, 2000, **2**, 3237–3240.
34 D. Boeglin, S. Cantel, A. Heitz, J. Martinez and J. A. Fehrentz, *Org. Lett.*, 2003, **5**, 4465–4468.
35 S. Dahmen and S. Bräse, *Org. Lett.*, 2000, **2**, 3563–3565.
36 G. Hennrich, W. Walther, U. Resch-Genger and H. Sonnenschein, *Inorg. Chem.*, 2001, **40**, 641–644.
37 C. C. Cheng, Z. S. Chen, C. Y. Wu, C. C. Lin, C. R. Yang and Y. P. Yen, *Sens. Actuators, B*, 2009, **142**, 280–287.
38 B. Liu and H. Tian, *Chem. Commun.*, 2005, 3156–3158.
39 A. Tsuge, T. Moriguchi, S. Mataka and M. Tashiro, *J. Chem. Soc., Perkin Trans. 2*, 1993, 2211–2215.
40 The X-ray crystallographic data for probe 1 has been submitted to Cambridge crystallography Data Center (CCDC No. 1859342)†.
41 H. Zhou, C. Xue, P. Weis, Y. Suzuki, S. Huang, K. Koynov, G. K. Auernhammer, R. Berger, H. J. Butt and S. Wu, *Nat. Chem.*, 2017, **9**, 145–151.
42 M. Dong, A. Babalhavaeji, S. Samanta, A. A. Beharry and G. A. Woolley, *Acc. Chem. Res.*, 2015, **48**, 2662–2670.
43 S. Guo, K. Matsukawa, T. Miyata, T. Okubo, K. Kuroda and A. Shimojima, *J. Am. Chem. Soc.*, 2015, **137**, 15434–15440.
44 H. D. Bandara and S. C. Burdette, *Chem. Soc. Rev.*, 2012, **41**, 1809–1825.
45 A. A. Beharry and G. A. Woolley, *Chem. Soc. Rev.*, 2011, **40**, 4422–4437.
46 G. K. Joshi, K. N. Blodgett, B. B. Muhoberac, M. A. Johnson, K. A. Smith and R. Sardar, *Nano Lett.*, 2014, **14**, 532–540.
47 Y. Nabetani, H. Takamura, Y. Hayasaka, T. Shimada, S. Takagi, H. Tachibana, D. Masui, Z. Tong and H. Inoue, *J. Am. Chem. Soc.*, 2011, **133**, 17130–17133.
48 I. V. Malyar, E. Titov, N. Lomadze, P. Saalfrank and S. Santer, *J. Chem. Phys.*, 2017, **146**, 104703.
49 D. A. Paterson, J. Xiang, G. Singh, R. Walker, D. A. M. Agra-Kooijman, A. Martínez-Felipe, M. Gao, J. M. Storey, S. Kumar and O. D. Lavrentovich, *J. Am. Chem. Soc.*, 2016, **138**, 5283–5289.
50 A. M. Kolpak and J. C. Grossman, *Nano Lett.*, 2011, **11**, 3156–3162.
51 J. Wei, Y. Liu, J. Chen, Y. Li, Q. Yue, G. Pan, Y. Yu, Y. Deng and D. Zhao, *Adv. Mater.*, 2014, **26**, 1782–1787.
52 Z. Wu, R. Xue, M. Xie, X. Wang, Z. Liu, M. Drechsler, J. Huang and Y. Yan, *J. Phys. Chem. Lett.*, 2017, **9**, 163–169.
53 J. Choi, W. Cho, Y. S. Jung, H. S. Kang and H. T. Kim, *ACS Nano*, 2017, **11**, 1320–1327.
54 A. Rezaee, J. Derayat, S. Mortazavi, Y. Yamini and M. Jafarzadeh, *Am. J. Environ. Sci.*, 2005, **1**, 102–105.
55 B. V. Tangahu, S. Abdullah, S. Rozaimah, H. Basri, M. Idris, N. Anuar and M. Mukhlisin, *Int. J. Chem. Eng.*, 2011, **2011**, 939161.
56 G. Qiu, X. Feng, P. Li, S. Wang, G. Li, L. Shang and X. Fu, *J. Agric. Food Chem.*, 2008, **56**, 2465–2468.
57 A. Oladele and O. Fadare, *Ethiop. J. Environ. Stud. Manage.*, 2015, **8**, 451–463.

58 K. H. Bishop, Y. H. Lee, J. Munthe and E. Dambrine, *Biogeochemistry*, 1998, **40**, 101–113.
59 Z. Wei, G. Wu, R. Su, C. Li and P. Liang, *Environ. Toxicol. Chem.*, 2011, **30**, 1997–2003.
60 M. Lodenius, E. Tulisalo and A. Soltanpour-Gargari, *Sci. Total Environ*, 2003, **304**, 169–174.
61 S. K. Vashist, O. Mudanyali, E. M. Schneider, R. Zengerle and A. Ozcan, *Anal. Bioanal. Chem.*, 2014, **406**, 3263–3277.
62 D. Tseng, O. Mudanyali, C. Oztoprak, S. O. Isikman, I. Sencan, O. Yaglidere and A. Ozcan, *Lab Chip*, 2010, **10**, 1787–1792.
63 P. Preechaburana, M. C. Gonzalez, A. Suska and D. Filippini, *Angew. Chem.*, 2012, **124**, 11753–11756.
64 S. O'Driscoll, B. D. MacCraith and C. S. Burke, *Anal. Methods*, 2013, **5**, 1904–1908.
65 Q. Wei, H. Qi, W. Luo, D. Tseng, S. J. Ki, Z. Wan, Z. N. Gorocs, L. A. Bentolila, T. T. Wu and R. Sun, *ACS Nano*, 2013, **7**, 9147–9155.